PAN
POLISH ACADEMY OF SCIENCES

Opto-Electronics Review

journal homepage: https://journals.pan.pl/opelre

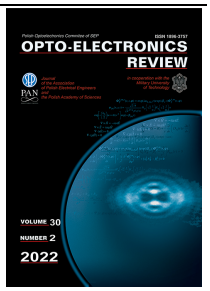

The determination of the carriers recombination parameters based on the HOT HgCdTe current-voltage characteristics

Tetiana Manyk[a*], Jarosław Rutkowski[a], Paweł Madejczyk[a], Waldemar Gawron[a,b], Piotr Martyniuk[a]

[a] Institute of Applied Physics, Military University of Technology, 2. Kaliskiego St., 00-908 Warsaw, Poland
[b] VIGO System S.A., 129/133 Poznańska St., 05-850 Ożarów Mazowiecki, Poland

Article info

Article history:
Received 25 Feb. 2022
Received in revised form 7 Apr. 2022
Accepted 27 Apr. 2022
Available on-line 30 May 2022

Keywords:
HgCdTe; MWIR detectors; dark current; *I-V* characteristics; recombination.

Abstract

A theoretical analysis of the mid-wavelength infrared range detectors based on the HgCdTe materials for high operating temperatures is presented. Numerical calculations were compared with the experimental data for HgCdTe heterostructures grown by the MOCVD on the GaAs substrates. Theoretical modelling was performed by the commercial platform SimuAPSYS (*Crosslight*). SimuAPSYS fully supports numerical simulations and helps understand the mechanisms occurring in the detector structures. Theoretical estimates were compared with the dark current density experimental data at the selected characteristic temperatures: 230 K and 300 K. The proper agreement between theoretical and experimental data was reached by changing Auger-1 and Auger-7 recombination rates and Shockley-Read-Hall carrier lifetime. The level of the match was confirmed by a theoretical evaluation of the current responsivity and zero-bias dynamic resistance area product (R_0A) of the tested detectors.

1. Introduction

The development of a variable bandgap ternary compound based on the mercury cadmium telluride $Hg_{1-x}Cd_xTe$ (HgCdTe) has started in 1959 by Lawson *et al.* [1]. HgCdTe exhibits a zinc blende crystal structure. The ability to vary the HgCdTe bandgap energy (E_g), by changing the cadmium molar composition (x), makes it possible to use HgCdTe for over the entire infrared radiation (IR) range (by changing the Hg/Cd ratio): short-wavelength IR (SWIR) with cut-off wavelength, $\lambda_{cut\text{-}off}$ = 1–3 µm, mid-wavelength IR (MWIR) with $\lambda_{cut\text{-}off}$ = 3–8 µm, long-wavelength IR (LWIR) with $\lambda_{cut\text{-}off}$ = 8–14 µm, and very long-wavelength IR (VLWIR) with $\lambda_{cut\text{-}off}$ = 14–30 µm [2–4]. The progress in the ternary material – HgCdTe as the most important intrinsic semiconductor for IR technology has been well known. The HgCdTe has been considered as the main optoelectronic material/compound for IR detection exhibiting excellent electro-optical properties, showing high detectivity (D^*) and quantum efficiency (QE) [5]. The HgCdTe properties allow for the devices design optimized for the SWIR, MWIR, and LWIR ranges [6]. The HgCdTe-based detectors have been used for a wide range of applications including military, industry, medicine, and broadly defined science and technology [7]. Although the ternary HgCdTe has been known and thoroughly researched for a long period of time, that material still exhibits minor problems. The most important and commonly present in the metal-organic chemical vapour deposition (MOCVD) technology are point defects resulting from the weak Hg–Te bonds, causing residual acceptors on the surface [6].

The high optical absorption allows for the fabrication of high QE HgCdTe-based IR detectors. Current research efforts are focused on double-layer heterojunction photodiodes where a narrow bandgap p-type base layer is sandwiched between two highly doped contact layers $N^+/p/P^+$ (the capital letter denotes the wider gap regions, sign + denotes the high doping level). The bandgap of the N^+ and P^+ layers should be large enough to make thermal generation low and to prevent electrons injection into the absorber region. The main advantages of these detectors are response time and high signal-to-noise ratio. In addition, the detector performance in the long term/time stability should be an important figure of merit.

For many years, the parameters of various photovoltaic detectors, especially their current-voltage (I-V) character-

*Corresponding author at: tetjana.manyk@wat.edu.pl

https://doi.org/10.24425/opelre.2022.141596
1896-3757/ Association of Polish Electrical Engineers (SEP) and Polish Academic of Sciences (PAS). Published by PAS

istics, have been studied and analysed [8–10]. Many concepts have been proposed to improve the HgCdTe infrared detector performance and to reach high operating temperature (HOT) conditions [11].

Apart from photoconductive detectors and photodiodes [6], photoelectromagnetic detectors [12] were an effective solution. A significant improvement in the reduction of the dark current was achieved by suppressing the Auger thermal generation using nonequilibrium conditions of a device operation [13]. New methods used to create HOT detectors include barrier structures, for example nBn [14, 15]. MOCVD allows for a controlled growth of HgCdTe heterostructures with almost any doping, energy bandgap profile, and precisely controlled graded interfaces. The performance of HOT LWIR HgCdTe avalanche photodiodes (APDs) is significantly limited by the increasing dark current associated with the detector operation at high temperatures. By coupling the structure of the barrier layer in the APD, it is possible to effectively reduce the carrier concentration in the absorption area [16]. The photodiode saturation currents suppression was reached in various ways, mainly by the generation-recombination (GR) processes reduction occurring in the detector active areas. The problem of the contribution and significance of individual GR effects for the HgCdTe-based devices is still open and unsolved.

In this paper, a theoretical analysis of the MWIR HgCdTe-based structures designed for the HOT conditions is presented. The work shows the match between experimental and theoretical data by implementation of the corrected Auger and Shockley-Read-Hall (SRH) GR coefficients. Theoretical modelling was performed by the commercial program SimuAPSYS (*Crosslight*). That platform supports numerical simulations and helps understand the effects occurring within detector structures.

2. Photodiode design and theoretical simulation

The HgCdTe heterostructure epitaxial growth was performed in the AIX-200 Aixtron horizontal reactor by the MOCVD method. A description of the MOCVD system and the growth process was presented in the authors' previous papers [17, 18]. The standard processing/technology was applied to the fabrication of the HgCdTe IR photodiodes on a GaAs substrate designed to work at temperatures close to 300 K (HOT conditions). The analysed samples consist of two contact layers (CL), two transient layers (TL), and a *p*-type doped active (absorber) layer (AL). The designed structure differs from the classical photodiode ($N^+/p/P^+$) by an extra transient layers to shape an interface between the *p*-type and both contact layers, preventing the formation of unfavourable potential barriers in the valence band. The above-described layers of the investigated detection structures were deposited in the following order: CL/TL/AL/TL/CL.

In this paper, two structures designed for the MWIR spectral range marked as Sample-1 and Sample-2 were compared. The layers sequence is the same in both samples, while the constituent layers differ in the thickness and doping concentration (Cd molar composition varies according to the assumed bandgap energy). For Sample-1, Cd molar composition assumes $x = 0.22$ and for Sample-2, $x = 0.29$, contributing to the cut-off wavelengths $\lambda_{\text{cut-off}} = 6.7$ µm and 4.2 µm at 300 K, respectively. Table 1 presents the parameters of the tested devices.

Table 1.
Structural parameters used in the simulation.

Region	Doping concentration (cm^{-3})	Thickness (µm)	Cd mole fraction
Sample-1			
P^+ – Contact layer	2.0×10^{17}	0.8	0.31
p – Transient layer	1.0×10^{16}	0.7	0.30–0.22
p – Active layer	3.5×10^{15}	5.1	0.22
n – Transient layer	1.0×10^{16}	1.6	0.36–0.40
N^+ – Contact layer	2.0×10^{17}	8.9	0.40
Sample-2			
P^+ – Contact layer	5.0×10^{17}	2.2	0.54
p – Transient layer	5.0×10^{15}	0.9	0.37–0.29
p – Active layer	3.0×10^{15}	4.0	0.29
n – Transient layer	1.0×10^{16}	0.5	0.33–0.48
N^+ – Contact layer	2.0×10^{17}	9.3	0.48

2.1. Experimental data

The current-voltage and spectral characteristics of the tested photodiodes were measured within the temperature range of 200–300 K.

Figure 1 shows the spectral current responsivity (R_i) experimental data *vs*. the wavelength at 300 K (the bias voltage was $U = -100$ mV). Sample-1 exhibits 2 times higher maximum responsivity than Sample-2 due to the longer cut-off wavelength and higher quantum efficiency.

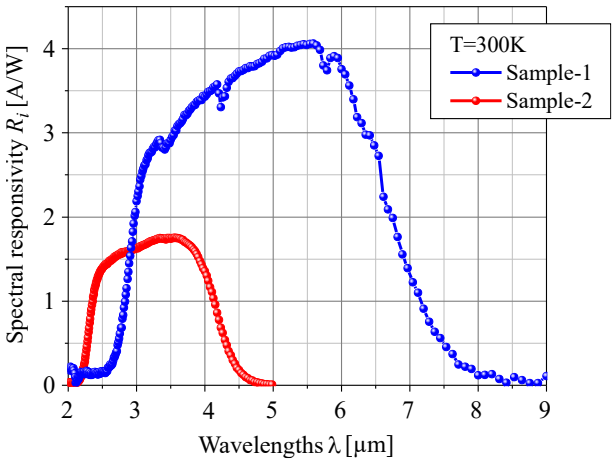

Fig. 1. The spectral current responsivity (R_i) experimental data for Sample-1 and Sample-2 at 300 K ($U = -100$ mV).

The dark current density (J_d) experimental data *vs*. voltage for Sample-1 and Sample-2 at 300 K are shown in Fig. 2. The reverse saturation current in the longwave detector (Sample-1) is more than two orders of magnitude greater than the saturation current in Sample 2. An increase in the impact of Auger recombination *vs*. decreasing energy gap (negative difference resistance for Sample-1) is an

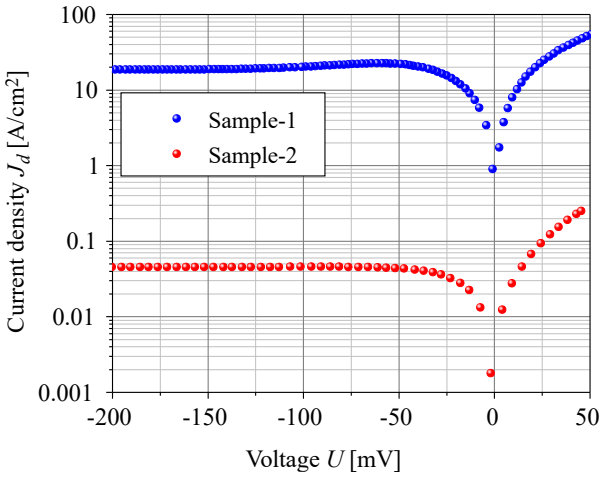

Fig. 2. The dark current density (J_d) experimental data for Sample-1 and Sample-2 at 300 K.

interesting effect for the theoretical research to determine the recombination parameters of the tested devices.

The analysis of J_d *vs.* temperature shows the activation energy (E_a) dependence estimated according to the expression

$$J_d \sim e^{-(E_a/k_B T)}, \quad (1)$$

where T is the temperature and k_B is the Boltzmann constant. Arrhenius plot, presented in Fig. 3 for Sample-1 and Sample-2, shows that activation energies at high temperatures equal $E_a = 146$ meV and $E_a = 182$ meV, respectively. At high temperatures, the device (Sample-1) exhibited a thermal activation energy close to that of the bandgap energy demonstrating a significant suppression of SRH contributions (confirming that the dark current at higher temperatures is mostly due to the diffusion component). In the case of Sample-2, the value of the thermal activation energy is close to 0.7 E_g. It means that the GR current is mostly generated by the SRH recombination process.

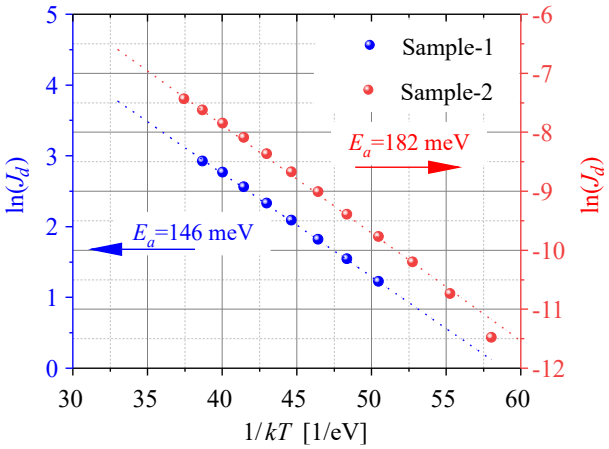

Fig. 3. Arrhenius plot for Sample-1 and Sample-2.

2.2. *Theoretical simulation*

Numerical simulations of the HgCdTe multilayer heterostructure were performed by the commercial platform SimuAPSYS (*Crosslight Inc.*). The numerical model implemented in the APSYS platform uses GR mechanisms in HgCdTe. All equations describing GR models and parameters as intrinsic carrier concentration, bandgap energy, carrier mobility, dielectric constants used in the simulations were taken mainly from the Capper's monograph and the APSYS manual [19, 20].

Figure 4 shows the energy band structure of the investigated device (Sample-1) under the reverse voltage $U = 0.2$ V (E_F, E_c, E_v are the Fermi level, conduction band, and valence band energies, respectively). For Sample-2, the shape of the band structure is similar.

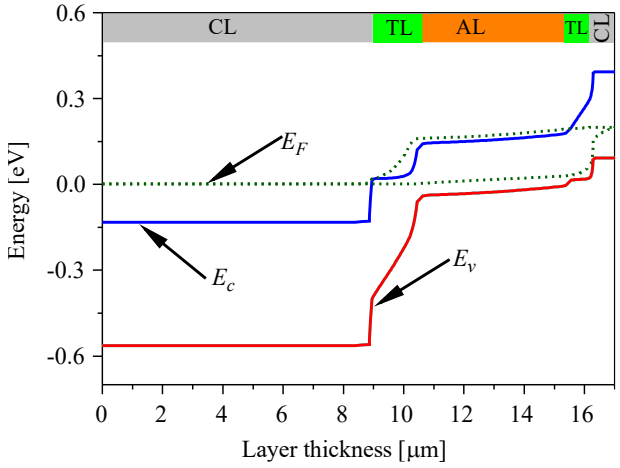

Fig. 4. The energy band structure for Sample-1 *vs.* device profile under reverse voltage $U = 0.2$ V.

The linear gradients of the Cd molar composition and doping were assumed allowing to eliminate the barrier arising in the valence band (at zero voltage). This approach was used to suppress undesirable discontinuities in energy bands influencing the carrier transport. In fact, the gradients in the transition layers stemming from the Hg interdiffusion during the MOCVD deposition of the consecutive layers are not exactly known. The detectors were illuminated from the N^+ side layer (wider bandgap material) with the light power at the level of $P = 50$ W/m^2 (the wavelength light for Sample-1 is 4 μm and for Sample-2 equals 6 μm).

The non-fundamental carrier lifetime in the semiconductor structures is an important parameter related to the diffusion length and diffusion coefficient (structural quality/uniformity) which affects detection parameters of the photosensitive device. Defects reduction in the epitaxial heterostructures leads to the need to analyse GR effects and the non-fundamental carrier lifetime [21–23].

Assuming bulk processes only, there are three main thermal GR mechanisms: SRH [24, 25], radiative, and Auger [26, 27]. The SRH mechanism occurs via levels in the energy bandgap being responsible for the carrier lifetimes in a lightly doped HgCdTe. The role of the radiative mechanism is reduced by the reabsorption of photons in the absorber layer so that GR processes are not important, especially for a longer wavelength (for Sample-1) [28]. The Auger effects are very important in narrow bandgap materials, since the probability of these processes increases sharply when the bandgap decreases. It is important to consider two components of the Auger mechanisms to include Auger-1 and Auger-7. The following formula is used to determine the net GR rate (considering Auger-1 and Auger-7 GR contribution):

$$R_{Aug} = \left(C_n n - C_p p\right)(np - n_i^2), \tag{2}$$

where n is the electron concentration, p is the hole concentration, n_i is the intrinsic carrier concentration, C_n and C_p are the Auger recombination coefficients (Auger-1 and Auger-7, respectively) which can be written by the equations [29, 30]:

$$C_n = \frac{8 \cdot (2\pi)^{2.5} \cdot q^4 \cdot m_0}{h^3 \cdot (4\pi\varepsilon_0\varepsilon_s)^2} \cdot \frac{(m_e/m_0) \cdot |F_{12}|^2}{n_i^2 \cdot (1+\mu)^{0.5} \cdot (1+2\mu)} \cdot \left(\frac{k_B T}{E_g}\right)^{1.5} \cdot e^{\left(-\frac{1+2\mu}{1+\mu} \cdot \frac{E_g}{k_B T}\right)}, \tag{3}$$

$$C_p = C_n/\gamma\,, \tag{4}$$

where q is the electron charge, m_0 is the free electron mass, F_{12} is the Auger overlap parameter (Bloch overlap integral), k_B is the Boltzmann constant, T is the temperature, E_g is the energy bandgap, m_e is the electron effective mass (conduction band), m_h is the heavy-hole effective mass (valence band), μ is the electron to the heavy-hole effective mass ratio, ε_0 and ε_s are the dielectric and static frequency dielectric constants. The γ parameter describing the Auger-7 to Auger-1 intrinsic times ratio is highly uncertain. Typical values are within the range of $3 < \gamma < 6$ [31] and for the purpose of this paper it was assumed at the level of $\gamma = 5$.

Using formulas (3) and (4) presented above, the C_n and C_p coefficients were assessed to be used for the device performance simulation. A theoretical analysis of the Auger and SRH GR contribution in the absorber layer on the HgCdTe-based devices performance was performed.

The theoretical results of the research on the Auger coefficients and the SRH carrier lifetime influence are presented based on the *I-V* characteristics fitting the procedure for Sample-2. Table 2 shows the selected Auger coefficients (C_n and C_p) and the SRH carrier lifetime (τ_n and τ_p) used in the theoretical calculations.

Table 2.
SRH carrier lifetime and Auger coefficients used in the theoretical simulation (Sample-2) at 300 K.

Case	SRH carrier lifetime		Auger coefficients	
	τ_n (μs)	τ_p (μs)	C_n (cm^6/s)	C_p (cm^6/s)
a	1.51	0.151	1.6×10^{-38}	3.2×10^{-39}
b	1.31	0.131	1.2×10^{-38}	2.4×10^{-39}
c	1.23	0.123	1.0×10^{-38}	2.0×10^{-39}
d	1.20	0.120	0.9×10^{-38}	1.8×10^{-39}
e	1.00	0.100	0.8×10^{-38}	1.36×10^{-39}

The theoretical simulations show that the SRH lifetime significantly affects the photodiode saturation current density, while the Auger GR factor determines the shape of the *I-V* curves near $U \to 0$ V. Figure 5 shows the *I-V* characteristics *vs*. reverse voltage for the HgCdTe detector (Sample-2) for selected Auger and SRH GR coefficients at 300 K.

The Auger GR coefficients and the SRH carrier lifetime were selected to reach the saturation current density at the experimental level of 0.045 A/cm^2. The analysis of the GR coefficients influence on the *I-V* characteristics allows to conclude that the Auger suppression increases when the Auger and SRH GR rates are comparable. When the SRH GR rate is the highest (lifetime is the shortest – case "e"), the Auger suppression effect is invisible on the *I-V* characteristics. Auger suppression in HOT HgCdTe devices translates into a unique negative differential resistance in the reverse bias *I-V* characteristics, and in order to control it, the correct ratio between the Auger and SRH GR should be maintained.

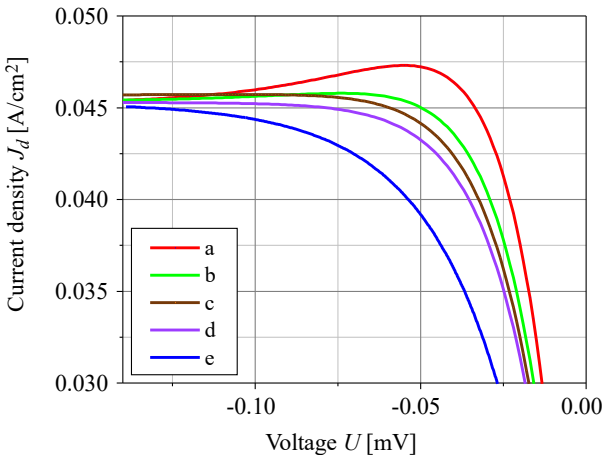

Fig. 5. Sample-2 *I-V* characteristics *vs*. reverse voltage for the selected Auger and SRH GR coefficients at 300 K (see Table 2).

The GR rates are shown in Fig. 6. The Auger processes play a major role in limiting the HgCdTe performance of infrared photodiodes at the low reverse voltage. At a reverse bias higher than 70 mV, SRH processes become the limiting mechanisms.

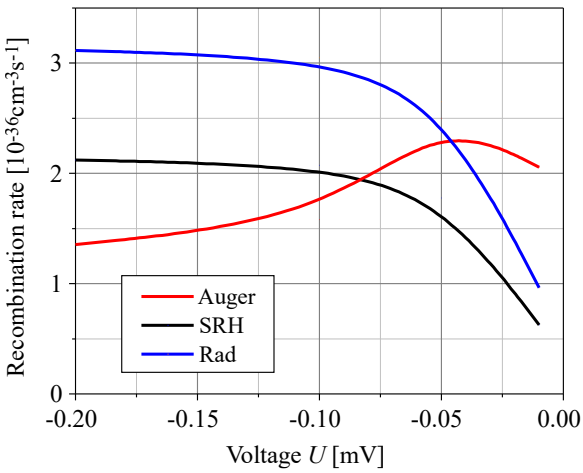

Fig. 6. Theoretically calculated GR rates for SRH, radiative, and Auger processes at 300 K *vs*. reverse voltage for Sample-2 for GR coefficients denoted by the symbol "d" in Table 2.

The GR rates corresponding to the SRH, radiative, and Auger processes *vs*. device profile for Sample-2 at 300 K are shown in Fig. 7 ($U = -0.2$ V). It can be seen that a recombination occurs in the region of the absorber and transition layer, and the rate of SRH is higher than that of Auger. In the junction area, a slight increase in the rate of SRH GR compared to the area of the absorber is observed. The dependence between SRH and Auger GR for Sample-1 is similar.

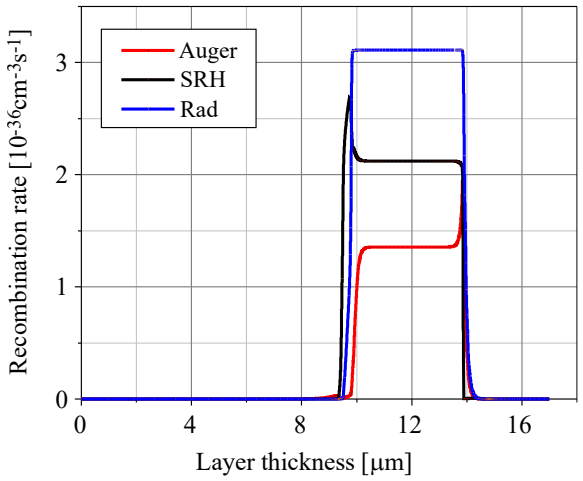

Fig. 7. Theoretically calculated SRH, radiative, and Auger GR rates for Sample-2 at 300 K for GR coefficients denoted by the symbol "d" in Table 2 ($U = -0.2$ V).

2.3. *Theoretical fit of current-voltage characteristics*

The proper selection of the GR rates allows fitting to the experimental *I-V* characteristics. Figure 8 shows the fitting of the theoretically simulated *I-V* curves of Sample-2 to the experimental characteristics at 300 K, obtained for the GR coefficients marked by the symbol "d". The fitting procedure assumed a detector series resistance at the level of $R_sA = 0.05\ \Omega\cdot\text{cm}^2$.

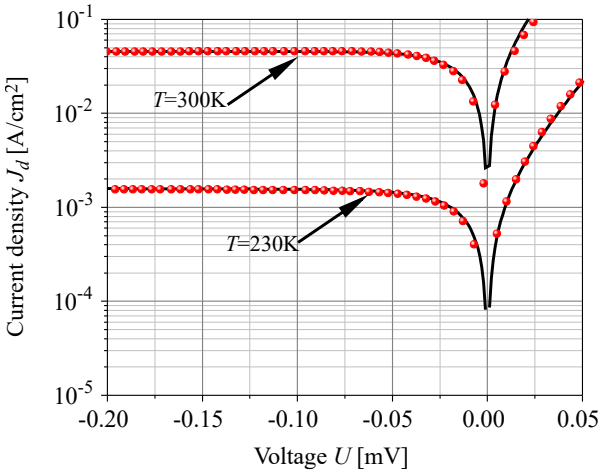

Fig. 8. Theoretical fit of Sample-2 *I-V* characteristics at $T = 230$ K and $T = 300$ K for GR coefficients denoted by the symbol "d" in Table 2.

A similar fitting between theoretical and experimental characteristics was performed for Sample-1. Figure 9 shows dependence of the *I-V* curves (matching of theory and experiment) for HOT conditions. The proper agreement between theory and experiment was achieved in the analysed temperature range (circles depict the measured data and lines present the theoretical simulations, respectively).

The GR coefficients used for device simulations are presented in Table 3. The Auger GR coefficients (C_n and C_p) were determined assuming $F_{12} = 0.10$–0.30. The Auger overlap parameter F_{12} decreases *vs*. bandgap energy. When the absorber energy bandgap decreases, the Auger GR contribution increases (C_n and C_p coefficients increase and

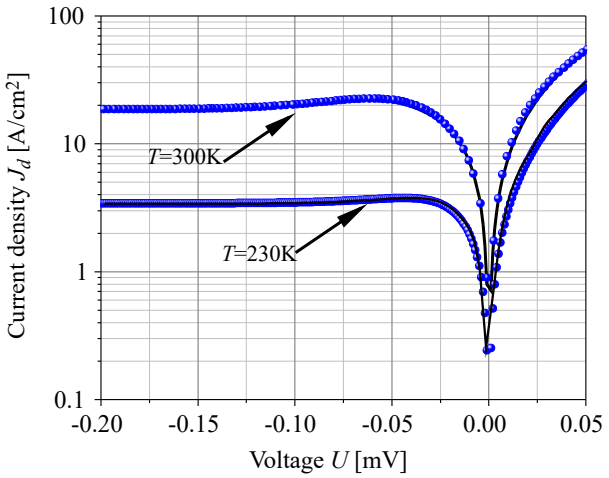

Fig. 9. Theoretically calculated and measured *I-V* curves of Sample-1 for HOT temperatures: 230 K and 300 K.

the Auger overlap parameter F_{12} increases within the range from 0.22 for Sample-2 to 0.30 for Sample-1) and the influence of recombination through SRH centres decreases (SRH carrier lifetime increases).

Table 3.
SRH carrier lifetime and Auger coefficients used in the simulation.

Sample	T (K)	SRH carrier lifetime		Auger coefficients	
		τ_n (μs)	τ_p (μs)	C_n (cm^6/s)	C_p (cm^6/s)
1	230	13.40	1.34	1.80×10^{-37}	3.59×10^{-38}
	300	13.40	1.34	4.00×10^{-38}	8.01×10^{-39}
2	230	1.20	0.12	1.37×10^{-38}	2.73×10^{-39}
	300	1.20	0.12	8.39×10^{-39}	1.68×10^{-39}

The theoretical analysis allowed to assess the zero-voltage dynamic resistance area product (R_0A) (see Table 4). The quality of the fit was confirmed by the proper agreement of the theoretical and experimental R_0A product data.

Table 4.
Theoretically and experimentally determined R_0A product.

Sample	T (K)	R_0A ($\Omega\cdot\text{cm}^2$)	
		theor.	exp.
1	230	4.11	3.96
	300	1.23	1.27
2	230	41.2	38.1
	300	3.8	4.5

Sample-1 and Sample-2 current responsivities *vs*. voltage are shown in Fig. 10. Theoretical dependence (solid line) was compared with the experimental data (circle). In the case of Sample-2, the responsivity is practically constant and does not depend on the voltage. On the other hand, Sample-1 responsivity reaches its maximum at a reverse bias of 0.1 V and decreases strongly for unbiased conditions. Shapes of the theoretical and experimental curves shown in the figure are similar.

Sample-1 was designed for longer wavelengths than Sample-2 what contributes to the stronger Auger

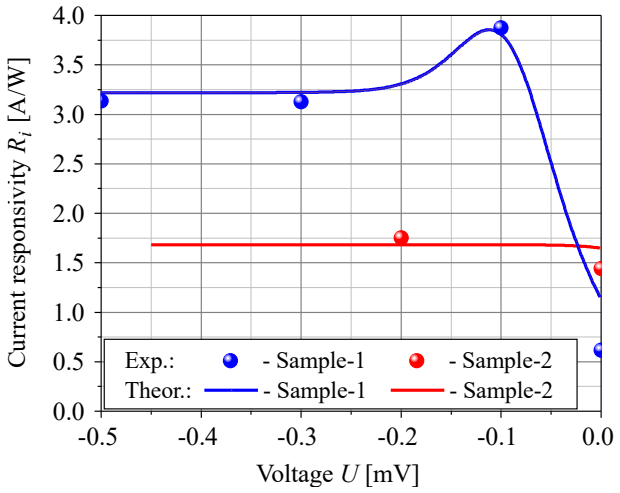

Fig. 10. Theoretical and experimental current responsivities *vs.* reverse voltage for Sample-1 ($\lambda = 6$ μm) and Sample-2 ($\lambda = 4$ μm) at 300 K.

suppression and the observed increase in current responsivity *vs.* reverse bias. Small potential barriers in the valence band in the transition layers should be considered, inhibiting the flow of charge carriers and, thus, reducing the detector *QE*. Those barriers decrease *vs.* voltage and the detector current responsivity increases.

3. Conclusions

The theoretical analysis of the MWIR HgCdTe detectors operating at HOT conditions was presented. Two samples with cut-off wavelengths within the MWIR range were selected for analysis and comparison. Theoretical simulation was performed by the commercial program SimuAPSYS. Numerical calculations were compared with the experimental data for the HgCdTe photodiodes. Theoretical estimates of the dark current were combined with the experimental data at 230 K and 300 K. The proper agreement of the theoretical and experimental data was reached by selection of the GR coefficients (C_n, C_p, and SRH). The method presented in the paper allows to determine the GR parameters of the analysed devices by the theoretical *I-V* curves fitting to the experimental data. The simulation results presented in the paper can provide theoretical support for further research on the HgCdTe detectors considering LWIR avalanche photodiodes.

Authors' statement

Research concept and design, T. M.; collection and/or assembly of data, P. M. and W. G.; data analysis and interpretation, J. R.; writing the article, T. M. and J. R.; critical revision of the article, P. M.; final approval of article, T. M., W. G., and P. M.

Acknowledgements

This work was supported by the National Science Centre (Poland), grant no. UMO-2019/33/B/ST7/00614; and by the National Centre for Research and Development grant no. RPMA.01.02.00-14-b451/18-00.

References

[1] Lawson, W. D., Nielson, S., Putley, E. H. & Young, A. S. Preparation and properties of HgTe and mixed crystals of HgTe-CdTe. *J. Phys. Chem. Solids* **9**, 325–329 (1959). https://doi.org/10.1016/0022-3697(59)90110-6

[2] Rogalski, A. HgCdTe infrared detector material: history, status and outlook. *Rep. Prog. Phys.* **68**, 2267–2336 (2005). https://doi.org/10.1088/0034-4885/68/10/r01

[3] Hansen, G. L., Schmit, J. L. & Casselman, T. N. Energy gap versus alloy composition and temperature in $Hg_{1-x}Cd_xTe$. *J. Appl. Phys.* **53**, 7099–7101 (1982). https://doi.org/10.1063/1.330018

[4] Harman, T. C. & Strauss, J. Band structure of HgSe and HgSe-HgTe alloys. *J. Appl. Phys.* **32**, 2265–2270 (1961). https://doi.org/10.1063/1.1777057

[5] Martyniuk, P. & Rogalski, A. Performance comparison of barrier detectors and HgCdTe photodiodes. *Opt. Eng.* **53**, 106105 (2014). https://doi.org/10.1117/1.OE.53.10.106105

[6] Rogalski, A. *Infrared and Terahertz Detectors.* (3rd ed.) (CRC Press Taylor & Francis Group, 2020). https://doi.org/10.1201/b21951

[7] Lei, W., Antoszewski, J. & Faraone L. Progress, challenges, and opportunities for HgCdTe infrared materials and Detectors. *Appl. Phys. Rev.* **2**, 041303 (2015). https://doi.org/10.1063/1.4936577

[8] Norton, P. HgCdTe infrared detectors. *Opto-Electron. Rev.* **10**, 159–174 (2002). https://optor.wat.edu.pl/10(3)159.pdf

[9] Qiu, W. C., Jiang, T. & Cheng, X. A. A bandgap-engineered HgCdTe PBπn long-wavelength infrared detector. *J. Appl. Phys.* **118**, 124504 (2015). https://doi.org/10.1063/1.4931661

[10] Iakovleva, N. I. The study of dark currents in HgCdTe heterostructure photodiodes. *J. Commun. Technol. Electron.* **66**, 368–374 (2021). https://doi.org/10.1134/S1064226921030220

[11] Martyniuk, P. & Rogalski, A. HOT infrared photodetectors. *Opto-Electron. Rev.* **21**, 240–258 (2013). https://doi.org/10.2478/s11772-013-0090-x

[12] Piotrowski, J. & Rogalski, A. Uncooled long wavelength infrared photon detectors. *Infrared Phys. Technol.* **46,** 115–131 (2004). https://doi.org/10.1016/j.infrared.2004.03.016

[13] Elliott, C. T. Non-equilibrium mode of operation of narrow-gap semiconductor devices. *Semicond. Sci. Technol.* **5**, S30–S37 (1990). https://doi.org/10.1088/0268-1242/5/3S/008

[14] Maimon, S. & Wicks, G. nBn detector, an infrared detector with reduced dark current and higher operating temperature. *Appl. Phys. Lett.* **89**, 151109 (2006). https://doi.org/10.1063/1.2360235

[15] Kopytko, M., Kębłowski , A., Gawron, W. & Pusz, W. LWIR HgCdTe barrier photodiode with Auger-suppression. *Semicond. Sci. Technol.* **31**, 035025 (2016). https://doi.org/10.1088/0268-1242/31/3/035025

[16] He, J. *et al.* Design of a bandgap-engineered barrier-blocking HOT HgCdTe long-wavelength infrared avalanche photodiode. *Opt. Express* **28**, 33556 (2020). https://doi.org/10.1364/OE.408526

[17] Gawron, W. *et al.* MOCVD Grown HgCdTe heterostructures for medium wave infrared detectors. *Coatings* **11**, 611 (2021). https://doi.org/10.3390/coatings11050611

[18] Kębłowski, A. *et al.* Progress in MOCVD growth of HgCdTe epilayers for HOT infrared detectors. *Proc. SPIE*. **9819**, 98191E-1 (2016). https://doi.org/10.1117/12.2229077

[19] APSYS Macro/User's Manual ver. 2011. Crosslight Software, Inc. (2011).

[20] Capper, P. P. *Properties of Narrow Gap Cadmium-Based Compounds*. (INSPEC, the Institution of Electrical Engineers, 1994).

[21] Long, F. *et al.* The structural dependence of the effective mass and Luttinger parameters in semiconductor quantum wells. *J. Appl. Phys.* **82**, 3414–3421 (1997). https://doi.org/10.1063/1.365657

[22] Lopes, V. C., Syllaios, A. J. & Chen, M. C. Minority carrier lifetime in mercury cadmium telluride. *Semicond. Sci. Technol.* **8**, 824–841 (1993). https://doi.org/10.1088/0268-1242/8/6s/005

[23] Aleshkin, V.Y. *et al.* Auger recombination in narrow gap HgCdTe/CdHgTe quantum well heterostructures. *J. Appl. Phys.* **129**, 133106 (2021). https://doi.org/10.1063/5.0046983

[24] Reine, M. B. *et al.* HgCdTe MWIR back-illuminated electron-initiated avalanche photodiode arrays. *J. Electron.* **36**, 1059–1067 (2007). https://doi.org/10.1007/s11664-007-0172-y

[25] Schuster, J. *et al*. Junction optimization in HgCdTe: Shockley-Read-Hall generation-recombination suppression. *Appl. Phys. Lett.* **107**, 023502 (2015). https://doi.org/10.1063/1.4926603

[26] Schacham, S. E. & Finkman, E. Recombination mechanisms in p-type HgCdTe: Freezeout and background flux effects. *J. Appl. Phys.* **57**, 2001–2009 (1985). https://doi.org/10.1063/1.334386

[27] Zhu, L. *et al*. Temperature-dependent characteristics of HgCdTe mid-wave infrared e-avalanche photodiode. *IEEE J. Sel. Top. Quantum Electron.* **28**, 3802709 (2022). https://doi.org/10.1109/JSTQE.2021.3121273

[28] Kopytko, M., Jóźwikowski, K., Martyniuk, P. & Rogalski, A. Photon recycling effect in small poxel p-i-n HgCdTe long wavelenght infrared photodiodes. *Infrared Phys. Technol.* **97**, 38–42 (2019). https://doi.org/10.1016/j.infrared.2018.12.015

[29] Olson, B. V. *et al*. Auger recombination in long-wave infrared InAs/InAsSb type-II superlattices. *Appl. Phys. Lett.* **107**, 261104 (2015). https://doi.org/10.1063/1.4939147

[30] Beattie, A. R. & Landsberg, P. T. Auger effect in semiconductors. *Proc. Math. Phys. Eng. Sci.* **A249**, 16−29 1959. https://doi.org/10.1098/rspa.1959.0003

[31] Krishnaumurthy, S. & Casselman, T. N. A detailed calculation of the Auger lifetime in p-type HgCdTe. *J. Electron. Mater.* **29**, 828−831 (2000). http://doi.org/10.1007/s11664-000-0232-z